A Photonic Front End for High Resolution Blue Spectral Sensor in 45 nm SOI SiPh Process

Md Nabil Shehtab Dhrubo, Jason Case, Agung Julius, Robert Karlicek, Mona Hella
Department of Electrical, Computer and Systems Engineering, Rensselaer Polytechnic Institute, Troy, NY 12180
Email: dhrubm@rpi.edu, casej3@rpi.edu, agung@ecse.rpi.edu, karlir@rpi.edu, hellam@rpi.edu

***Abstract*—A photonic front end for a blue spectral sensor in a standard silicon photonic process is presented. The detector is capable of identifying multiple spectral peaks within the blue wavelength range (410 nm $\sim$ 500 nm). The front end consists of grating structures with different grating pitches, followed by tapered waveguides. From the waveguide, the optical power is evanescently coupled to a silicon photodetector. To further improve the overall optical collection for the photodetector, an optical power combining network is also designed and optimized. The designs are fabricated using GlobalFoundries' 45SPCLO technology. The measurement results demonstrate the effect of varying the grating pitch in detecting different spectral peaks within the blue region, with peaks demonstrating responsivities ranging between 32$\sim$35 mA/W, depending on the grating pitch and the reverse bias.**

***Index Terms*—Silicon Photonics, Spectral Sensor, Circadian Rhythm, Blue Wavelength, Photonic Front End, Grating Couplers, Waveguide Tapers**

I. Introduction

CIRCADIAN rhythm evolved as a biological clock that synchronizes our biological processes with the light and dark pattern of the terrestrial day. The circadian rhythm is heavily linked to various physiological processes, including sleep, metabolism, hormone secretion, and neurobehavioral processes [1], [2]. Circadian rhythm disruption is known to have negative impacts on health, ranging from fatigue in frequent travelers with jetlag to an increased risk of cancer in rotating-shift workers.

Modern lifestyle poses a number of challenges in maintaining a healthy circadian rhythm, such as the proliferation of bright light during night time and remote working situations that blur the boundary between work and personal time. Numerous studies have suggested that excessive exposure to blue wavelengths disrupts circadian cycle the most [3], [4], [5]. The clinical standard for assessing circadian rhythm is by measuring biomarkers such as the concentration of hormones that participate in the circadian rhythm regulation. Off-the-shelf wearable devices partially fill the need for online personalized biometric measurements by recording a limited set of signals. However, this tends to exclude the critical measurement on blue light exposure.

Prior work [6], [7], [8], [9], [10] have demonstrated custom integrated circuit (IC) designs for multimodal biometric detection, including ExG (EEG / ECG / EMG) and arterial pulse waveform (APW). Such signals are considered indirect circadian phase marker. Attaching low power/small form factor custom multi-mode sensor ICs to a flexible substrate would reduce the weight of the wearable device (as shown in fig. 1(a,b)), ultimately increasing the comfort level of the user and allowing the use for extended periods of time. A block diagram of the proposed multi-modal biometric sensing platform for regulating circadian rhythm and neurocognitive performance is shown in fig. 1(c). It includes all the electrodes and sensors for bio-signal acquisition and post-processing circuits containing the analog front-end, a microcontroller unit, and a 433 MHz radio for wireless data transfer. An accelerometer is included to account for any body movement.

This work was supported by Division of Mathematical Sciences (DMS) of National Science Foundation (NSF) under Grant no. 2037357.

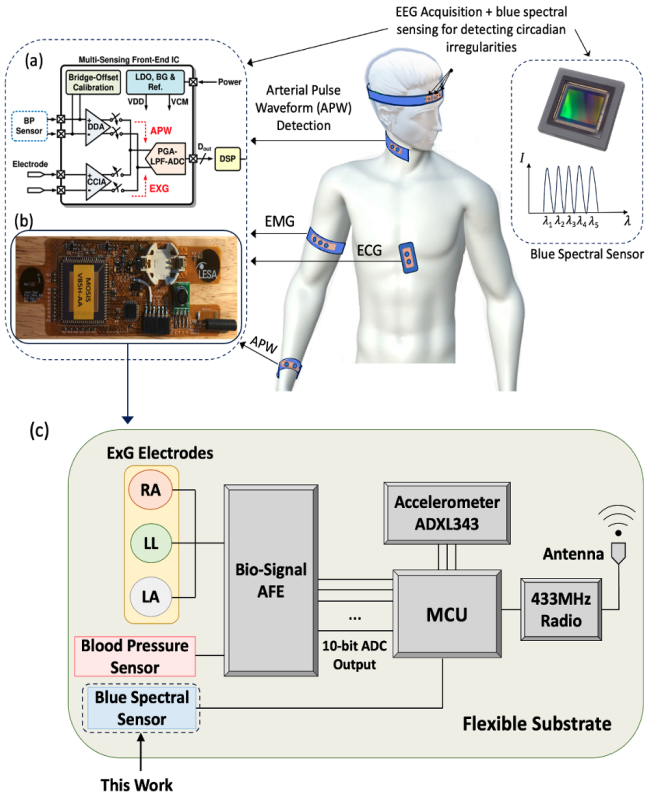

Fig. 1. Multi-modal biometric sensing platform for regulating circadian rhythm and neurocognitive performance: (a) block diagram of analog front-end IC to record ExG(EEG/EMG/ECG) and APW signals (figure reproduced from [11]), (b) printed circuit board on a flexible substrate with attached AFE IC, and (c) functional diagram of the sensor system (blue light sensor not currently included in the system).

To link the indirect circadian phase markers to blue light exposure, a light intensity measurement tool in the blue region needs to be added to the flexible substrate. Traditionally, blue-light sensing is conducted by using spectrometers or grating assisted photodiodes (PD). Spectrometers are typically bulky because of their complex optical path and components [12], [13], [14]. In this paper, we report on a grating assisted design of a spectral sensor in standard silicon photonic technology, capable of detecting multiple spectral peaks in the blue wavelength region.

Fig. 2 shows the unit pixel design of the spectral sensor with wavelength selective grating couplers, tapered waveguides, an optical power combining network and a photodiode. This pixel is designed using 45 nm SOI process design kit (PDK), known as 45SPCLO offered by GlobalFoundries Inc. The entire photonic front end is based of silicon nitride, which is located above the silicon layer. As a result, the optical power can be evanescently coupled from these nitride structures to a silicon photodetector. The pixel capabilities are demonstrated both through simulations and measurement results. The future phase of this work includes accumulating these pixels on a single chip, which will be attached to the flexible board shown in Fig. 1(b). Other than its use in regulating circadian rhythm, the combined multi-modal biometric data collection linked with blue light exposure can contribute to further understanding of the impact of artificial lighting on health and productivity.

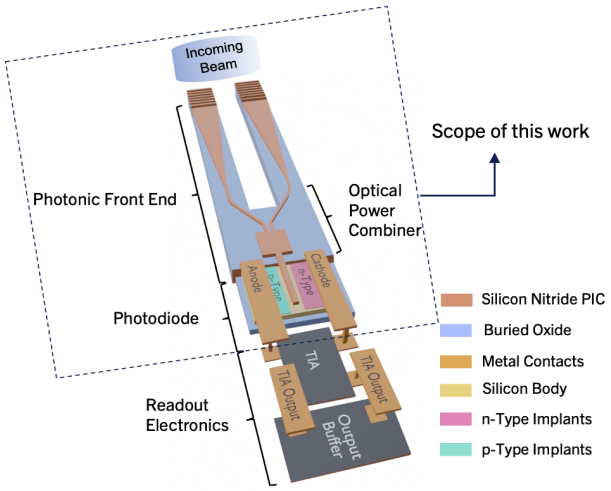

Fig. 2. Unit pixel of the proposed blue spectral sensor.

II. Device Design

A. Photonic Front End

The grating structures are optimized for maximum coupling of the detected wavelength to a tapered waveguide. The grating pitch is determined using the following expression [15]:

$$\Lambda = \frac{\lambda_0}{n_{eff} - n_E \sin(\theta)}, \tag{1}$$

where λ_0 is the central wavelength of Gaussian source, n_E is the refractive index of SiO_2, n_{eff} is the effective refractive index seen by the incoming beam and θ is the source incidence angle. The effective refractive index n_{eff} is determined by the fill factor (FF) of the gratings and is given as

$$n_{eff} = n_0(FF) + n_E(1 - FF), \tag{2}$$

where n_0 is the refractive index of Si_3N_4 at the given central wavelength. After determining grating pitch (Λ); width of each Si_3N_4 grating (W_0) and the width of the SiO_2 spacer (W_E) can be given as

$$W_0 = \Lambda(FF), \tag{3}$$

$$W_E = \Lambda(1 - FF). \tag{4}$$

Once the input optical modes are coupled in by the grating structures, they propagate through a linear adiabatic tapered waveguide. The lowest order optical mode is well confined by the sidewalls of the taper if the design conforms to the following inequality [16], [17] :

$$\alpha < \frac{\lambda_0}{2Wn_0}, \tag{5}$$

where W represents the taper width on both ends and α represents the taper angle. Assuming λ_0 to be 450 nm, waveguide width of 10 μm at the broader end and 0.8 μm at the narrower end, it can be shown that the taper angle needs to be within $0.62^o < \alpha < 7.8^o$ to fulfill the inequality in (5). Accordingly, the overall taper length needs to be in the range of 34 $\mu m <$ $L_{WG} <$ 425 μm. To verify this analysis, variational Finite-Difference-Time-Domain (FDTD) simulations are executed on the standalone tapered waveguide. For better area efficiency and to avoid selecting marginal value for taper length, values ranging between 70 μm and 110 μm are used for simulations. Fig. 3(b) shows transmission efficiency variation with these taper length values at different wavelengths within 360 nm $< \lambda_0 <$ 500 nm. For most wavelengths, simulations show maximum transmission for $L_{WG} = 90\mu m$, with transmission efficiency ranging within 88% ~95%.

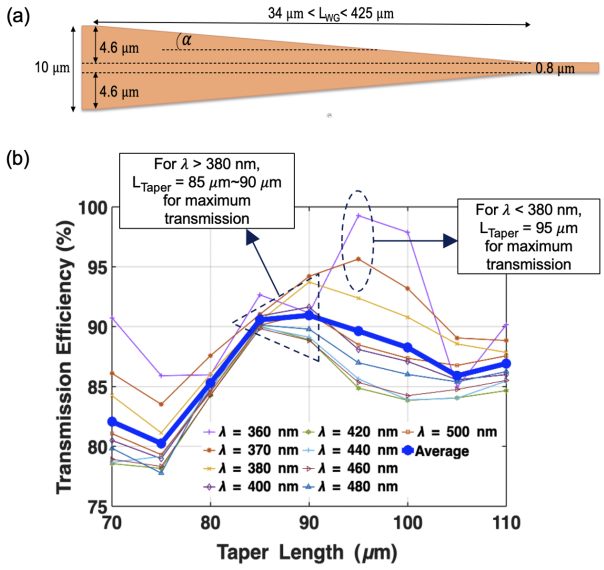

Fig. 3. (a) Illustration of tapered waveguide design, and (b) transmission efficiency variation with taper length.

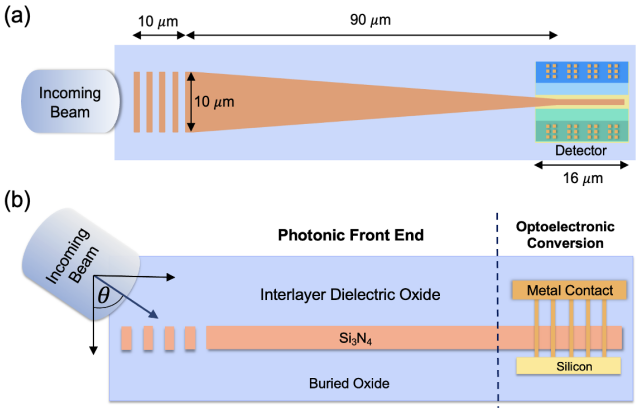

Fig. 4. (a) Top view, and (b) cross section of FDTD simulation setup.

In order to simulate this optimized tapered waveguide with grating couplers having different pitches, FDTD simulations are executed on the structure shown in Fig. 4. The coupling efficiencies of grating structures are simulated with grating pitches ranging within 660 nm $< \Lambda <$ 1187 nm. The grating structures can capture 8 different spectral peaks with coupling efficiencies varying between 23% $\sim$ 27% within 420 nm $< \lambda <$ 500 nm wavelength range, as shown in Fig. 5.

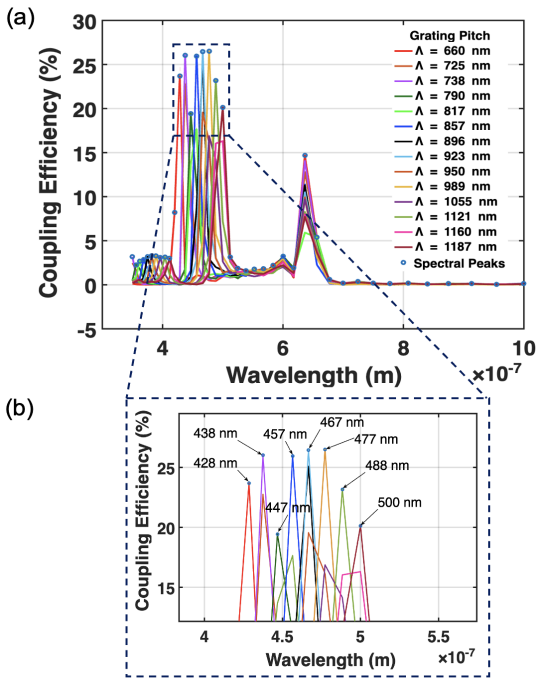

Fig. 5. (a) Simulated coupling efficiencies for different grating pitches, (b) Zoomed-in illustration of different spectral peaks.

B. Optical Power Combining Network

In order to increase the overall optical collection for the photodetector, combining optical signals from multiple photonic paths is required. Waveguide bends are added to route multiple signals towards a multi-mode interference (MMI) coupler. Fig. 6(a) shows the pixel design with a power combiner. Fig. 6(b),(c) show the FDTD simulation results for a 20^o bend with a lateral length of 62 μm, which shows around 3% propagation loss for 400 nm$\sim$500 nm wavelength range. In order to accumulate signals from the waveguide bends with maximum efficiency, the dimensions of the MMI coupler is optimized by implementing the self imaging principle [18]. Fig. 6(d),(e) show the simulated electric field profile and transmission efficiency of the MMI respectively for an optimized rectangular dimension of 21 μm $\times$ 3.5 μm. From the figure, it is evident that the transmissions into the input modes are identical (both close to 50%). The modes interfere constructively once inside the MMI and the second interference occurs very close to the output port, ensuring a strong transmission through the output waveguide (with $\sim$80% simulated transmission efficiency for 400 nm$\sim$500 nm wavelength range).

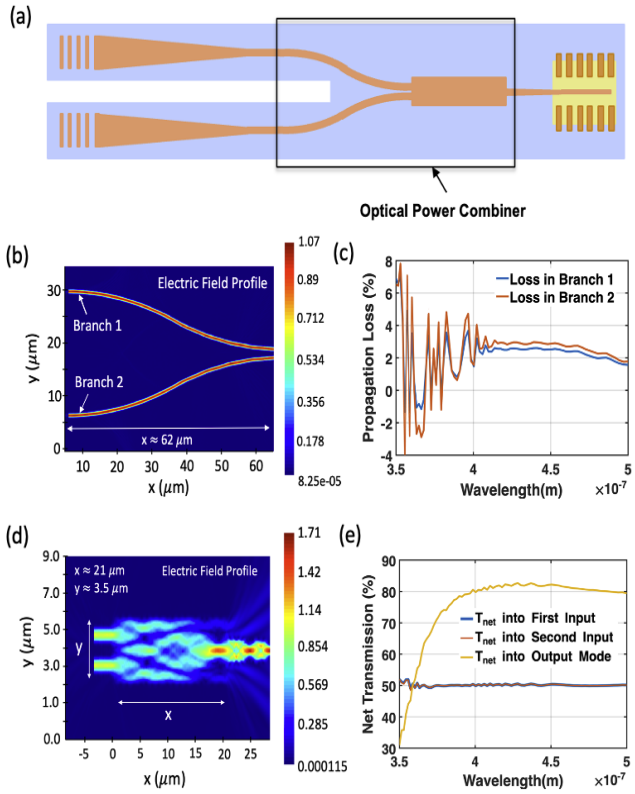

Fig. 6. (a) Top-view of a unit pixel with optical power combining network, (b) simulated electric field profile of a 20^o waveguide bend, (c) propagation loss profile for the bend, (d) simulated electric field profile of the optimized MMI coupler, and (e) net transmission profile for the MMI.

III. Experimental Results

The blue light sensor is fabricated in GlobalFoundries' 45SPCLO technology. Fig. 7(a) shows the microscopic image of wirebonded die while fig. 7(b) shows the die illuminated with a blue LED source. For testing the die, three LED sources with three different blue wavelengths (λ = 415 nm, 445 nm,

470 nm) are used. First, the LEDs were tested using a commercial spectrometer to determine their beam irradiance profiles, which helped to estimate the profiles of optical power incident on each grating. The incident power profiles for the three LEDs are shown in Fig. 7(c). These profiles were used to determine the responsivities of the silicon detectors coupled with different grating structures. Fig. 7(d) shows the measured dark current of silicon detectors upto a reverse bias of 5V. In general, the dark current is below 5 pA with the exception of only two detectors showing maximum dark current above 10 pA. Fig. 7(e),(f) and (g) shows the measured difference between photocurrent and dark current of these silicon detectors for LED wavelengths of 415 nm, 445 nm and 470 nm respectively. In these figures, Λ represents the different grating pitches to which these silicon detectors are coupled.

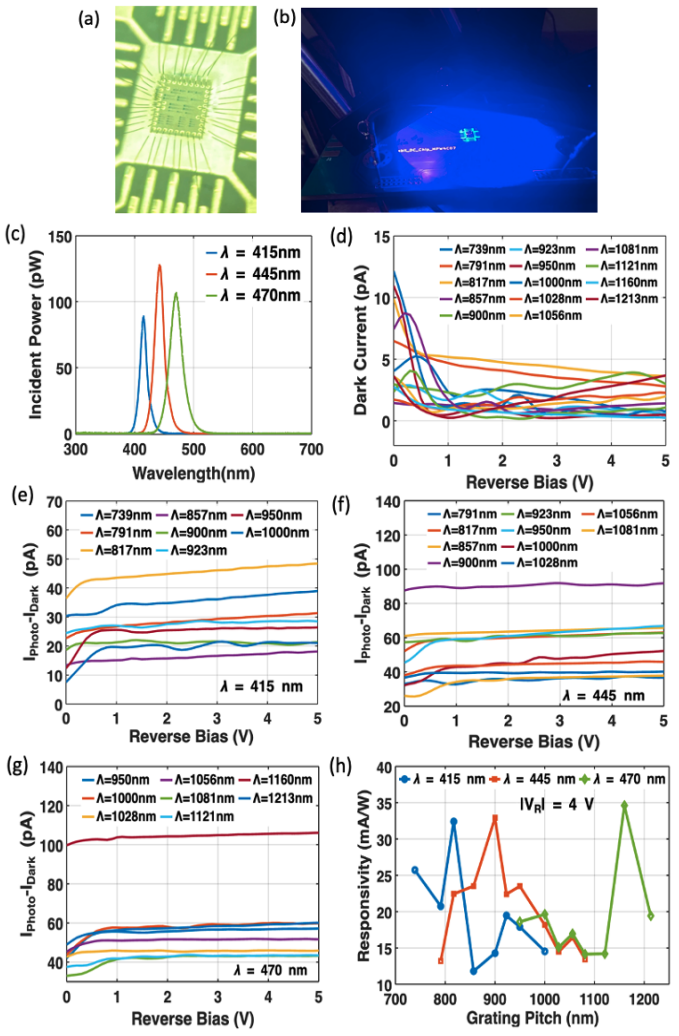

Fig. 7. (a) Die image; (b) Die illuminated with a blue LED source; (c)Measured profile of incident power on each grating; (d) Dark current characteristics of silicon detectors coupled to different grating structures; (e),(f),(g) Difference of photocurrent and dark current for these silicon detectors at 415 nm, 445 nm and 470 nm respectively; (h) Measured responsivities expressed as function of grating pitch for different wavelengths and $|V_R|$=4V

Finally, fig. 7(h) shows the measured responsivities of these silicon detectors as a function of grating pitch at 4V reverse bias. As expected from simulations, the smaller grating pitches (Λ <817 nm) respond better to the smallest wavelength (λ= 415 nm), the pitches between 857 nm and 950 nm show higher responsivity for 445 nm wavelength and the pitches above 1150 nm show higher responsivity for 470 nm wavelength. So, from both simulations and measurement results, it is verified that grating pitches roughly between 700 nm and 1200 nm with 30% fill factor should be sufficient to couple most of the spectral peaks within blue region.

The responsivities of silicon detectors coupled to optical power combiners were measured as well. Fig. 8 shows the responsivity improvement from one such detector, which receives combined power from grating pitches of 1121 nm and 1160 nm. Without the power combining network, at a reverse bias of 5V, the detector coupled to 1121 nm pitch demonstrates responsivity of ∼14 mA/W, while the detector coupled to 1160 nm pitch shows responsivity of ∼35 mA/W. The dark current of the detectors are negligible (as shown in Fig. 7(d)) and have insignificant effect on their responsivities. Thus, combining grating structures should result in almost 49 mA/W responsivity at $|V_R|$ = 5V. However, since the MMI coupler causes 20% transmission loss, the measured responsivity from the combined structure is around 40 mA/W.

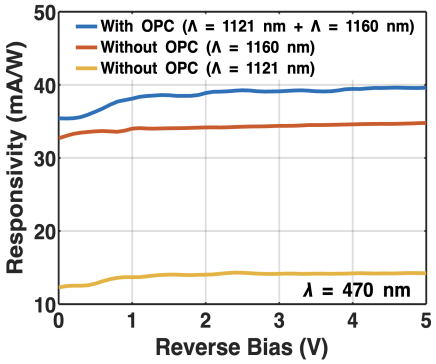

Fig. 8. Measured improvement in responsivity profiles for 470 nm wavelength due to using power combining network, accumulating power from grating pitches of Λ = 1121 nm and Λ = 1160 nm

IV. Conclusion

In conclusion, this work presents a photonic front end in a standard silicon photonic process that can successfully detect and filter multiple spectral peaks within the blue wavelength region. The device functions mostly based on grating pitch variation and its responsivity is improved using on-chip power combining. Light exposure with appropriate resolution between 400 nm - 500 nm wavelength is known to excite circadian rhythms. Combining blue-light spectral sensing and multimodal biometric measurements on a flexible substrate for wearables can contribute to further understanding and regulation of circadian rhythym and neurocognitive performance.

V. Acknowledgment

The authors would like to acknowledge GlobalFoundries Inc. for access to silicon fabrication through the 45SPCLO university program.

REFERENCES

[1] C.S.Pittendrigh, "Circadian rhythms and the circadian organization of living systems," Cold Spring Harb. Symp. Quant. Biol. , vol. 25, pp. 159-184, 1960, doi: 10.1101/sqb.1960.025.01.015.

[2] A. Martchenko, S. E. Martchenko, A. D. Biancolin, and P. L. Brubaker, "Circadian rhythms and the gastrointestinal tract: relationship to metabolism and gut hormones," Endocrinology, vol. 161, no. 12, Sep. 2020, doi:10.1210/endocr/bqaa167.

[3] J. H. Oh, H. Yoo, H. K. Park, and Y. R. Do, "Analysis of circadian properties and healthy levels of blue light from smartphones at night," *Sci. Rep.*, vol. 5, Jun. 2015, Art. no. 11325, doi:10.1038/srep11325.

[4] S. W. Lockley, G. C. Brainard, and C. A. Czeisler, "High sensitivity of the human circadian melatonin rhythm to resetting by short wavelength light," *J. Clin. Endocrinol. Metab.*, vol. 88, no. 9, pp. 4502–4505, Sep. 2003, doi:10.1210/jc.2003-030570.

[5] S. Wahl, M. Engelhardt, P. Schaupp, C. Lappe, and I. V. Ivanov,"The inner clock-blue light sets the human rhythm," *J. Biophotonics*, vol. 12, no. 12, Sep. 2019, Art. no. e201900102, doi:10.1002/jbio.201900102.

[6] Y. -P. Hsu, Z. Liu and M. M. Hella, "A 12.3-μW 0.72-mm^2 Fully Integrated Front-End IC for Arterial Pulse Waveform and ExG Recording," in *IEEE J. Solid-State Circuits*, vol. 55, no. 10, pp. 2756-2770, Oct. 2020, doi: 10.1109/JSSC.2020.3007177

[7] Y. -P. Hsu, Z. Liu and M. Hella, "A 10 $\mu\mathrm{W}-74.6\mathrm{dB}$ THD Arterial Pulse Waveform Sensing System with Automatic Bridge-Offset Calibration and Super Class-AB Output Stage," *2019 IEEE Asian Solid-State Circuits Conference (A-SSCC)*, Macau, Macao, 2019, pp. 297-300, doi: 10.1109/A-SSCC47793.2019.9056943.

[8] A. Dabbaghian and H. Kassiri, "An 8-Channel 0.45mm^2/Channel EEG Recording IC with ADC-Free Mixed-Signal In-Channel Motion Artifact Detection and Removal," *2020 IEEE International Symposium on Circuits and Systems (ISCAS)*, Seville, Spain, 2020, pp. 1-5, doi: 10.1109/ISCAS45731.2020.9181024.

[9] Y. -P. Hsu, Z. Liu and M. M. Hella, "A -68 dB THD, 0.6 mm^2 Active Area Biosignal Acquisition System With a 40–320 Hz Duty-Cycle Controlled Filter," *IEEE Transactions on Circuits and Systems I: Regular Papers*, vol. 67, no. 1, pp. 48-59, Jan. 2020, doi: 10.1109/TCSI.2019.2943904.

[10] M. S. Diab and S. A. Mahmoud,"14:5 nW; 30 dB Analog Front-End in 90-nm Technology for Biopotential Signal Detection," *2020 43rd International Conference on Telecommunications and Signal Processing (TSP)*, Milan, Italy, 2020, pp. 681-684, doi: 10.1109/TSP49548.2020.9163572.

[11] Y. -P. Hsu, Z. Liu and M. M. Hella, "A 12.3-μW 0.72-mm^2 Fully Integrated Front-End IC for Arterial Pulse Waveform and ExG Recording," in IEEE Journal of Solid-State Circuits, vol. 55, no. 10, pp. 2756-2770, Oct. 2020, doi: 10.1109/JSSC.2020.3007177.

[12] T. C. Wilkes, A. J. S. McGonigle, J. R. Willmott, T. D. Pering, and J. M. Cook, "Low-cost 3D Printed 1nm Resolution Smartphone Sensor-Based Spectrometer: Instrument Design and Application in Ultraviolet Spectroscopy," *Opt. Lett.*, vol. 42, no. 21, pp. 4323-4326, Nov. 2017, doi:10.1364/OL.42.004323

[13] S. Freer, A. Gorodetsky and M. Navarro-Cia, "Beam Profiling of a Commercial Lens-Assisted Terahertz Time Domain Spectrometer," *IEEE Trans. Terahertz Sci. Technol.*, vol. 11, no. 1, pp. 90-100, Jan. 2021, doi: 10.1109/TTHZ.2020.3026656.

[14] J.X.Y. Chew, Z.H.Lim, Y. Qi, G. Zhou, and G. Zhou, "High-throughput doubly-encoded single-pixel spectrometer with an extended aperture," *Opt. Express*, vol. 31, no. 15, pp. 24768-24784, Jul. 2023, doi:10.1364/OE.492382

[15] R. Marchetti, "High-efficiency grating-couplers: demonstration of a new design strategy," *Sci. Rep.*, vol. 7, Nov. 2017, Art. no. 16670, doi:10.1038/s41598-017-16505-z

[16] Y. Fu, T. Ye, W. Tang, and T. Chu, "Efficient adiabatic silicon-on-insulator waveguide taper," *Photon. Res.*. vol. 2, no. 3, pp. A41-A44, Jun. 2014, doi:10.1364/PRJ.2.000A41

[17] P. Sethi, A. Haldar, and S. K. Selvaraja, "Ultra-compact low-loss broadband waveguide taper in silicon-on-insulator," *Opt. Express*, vol. 25, no. 9, pp. 10196-10203, May. 2017, doi:10.1364/OE.25.010196

[18] S. Abdul-Majid, I. Hasan, P. Bock, and T. Hall, "Design, simulation and fabrication of a 90 degrees SOI optical hybrid based on the self-imaging principle," *Proc. SPIE - Int. Soc. Opt. Eng.*, vol. 7719, Apr. 2010, Art. no. 77190E, doi:10.1117/12.854735